A Numerical Investigation of Gain and Phase Errors of Unit Elements on Performance of Active Reconfigurable Intelligent Surface

Apisak Worapishet

Mahanakorn Institute of Innovation
Mahanakorn University of Technology
140 Cheumsamphan Road, Kratumrai, Nongchok, Bangkok, Thailand 10530
Email: apisak@mut.ac.th

Manuscript Received November 15, 2023
Revised December 1, 2023
Accepted December 8, 2023

ABSTRACT

A reconfigurable intelligent surface, particularly the active type, is recognized as a promising candidate to expand the coverage of 5G/6G wireless communication and beyond, thanks to its inexpensive implementation as compared to conventional infrastructures. In this paper, the impact of implementation errors on the performance of the surface is investigated by virtue of numerical computation. The analysis equations for calculating the incident field on the surface, and the reflected field as well as the far field pattern from the surface are outlined. Numerical simulation including the gain and phase variations associated with each unit cell are given at different sizes and phase resolutions of the surface. The performance errors are quantified and subsequently employed as a guideline for designing a reconfigurable surface with robust performance in practice.

Keywords: *Reconfigurable intelligent surface, passive reflector, active reflector, millimeter wave*

1. INTRODUCTION

A reconfigurable intelligent surface (RIS) has emerged as a cost effective candidate for expanding wireless communication coverage over the non-line-of-sight (nLOS) area as depicted in Fig. 1. This results in improving channel capacity performance of the next generation wireless communication technologies operating at GHz up to THz range, such as 5G/6G radios, without too excessive infrastructure cost [1].

An RIS is essentially a planar array of antenna elements, as represented by square patches in Fig. 1, which reflects and steers the impinging electromagnetic (EM) wave in the desired direction, particularly to the area of user elements (UE). Similar to the phase array antennas equipped at the base station (BS) antenna, the reflected EM beam from the RIS can also be scanned over the coverage area through individual control of the reflected phase in each antenna element by an electrically programmable means.

So far, the RIS implementation has been of a passive type in that it makes use of only a passive antenna element for EM wave reflection with no amplification [1] – [4]. However, its major drawback is attributed to the multiplicative path loss introduced by these passive RISs, which has a direct impact on the BS-to-UE and UE-to-BS nLOS link budgets [5]. This therefore adversely impacts and puts the fundamental limit on the BS-RIS-UE communication performance.

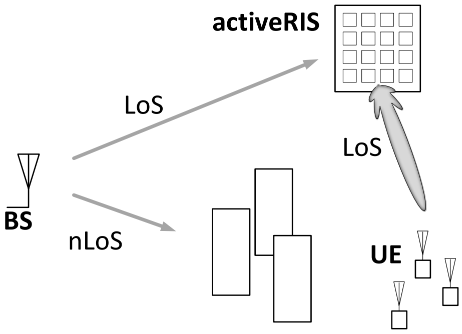

Fig. 1 *RIS for non-line-of-sight (nLOS) wireless communication area coverage*

Although, several remedies have been developed [2] – [5], such multiplicative path loss fundamentally imposes bottleneck on the performance of the BS-RIS-UE communication system.

Recently, theoretical investigations on communication performance of the so called “active” RIS, where each antenna element not only reflects but also amplify the incident EM waves via a reflection amplifier, has shown that the active RIS could potentially overcome the fundamental bottleneck due to the multiplicative fading [6] – [8]. For implementation in practice however, the electrical performance will be inevitably departed from ideal conditions assumed in the theoretical analysis, mainly due to errors from component tolerances and mismatches, as well as other physical limitations.

It is the purpose of this paper to investigate such practical impact by virtue of electromagnetic (EM) simulation of the active RIS taking into account two major variations including gain and phase errors due to the antenna and amplifier elements in each of the unit elements. In section 2, the analytical modelling equations governing the EM simulation of the active RIS and the phase distribution on the antenna array for steering the beam direction are summarized. This is followed by a description of the amplification element based on a negative-resistance type reflection amplifier. The models are then employed in Section 3 to investigate the impacts of gain and phase errors on the electrical parameters of the active RIS, including the peak directivity, steered direction, half-power beam width, and side-lobe levels. The implication of the results on practical implementation is also discussed, and conclusion will be given in Section 4.

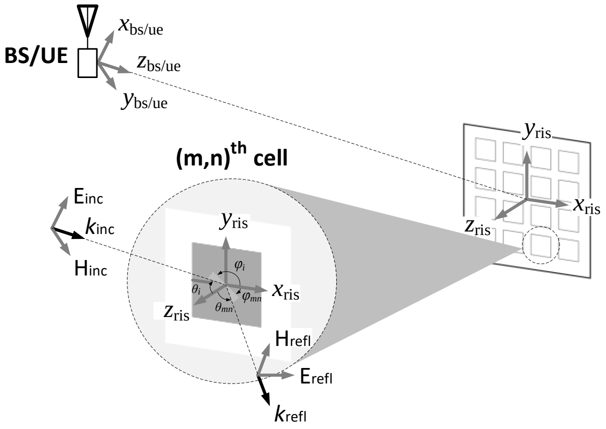

Fig. 2 *Diagram illustrating geometry and field of a BS antenna and an RIS*

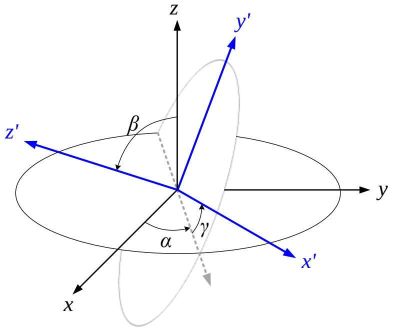

Fig. 3 *Cartesian co-ordinates related via Euclidean angles rotation (α, β, γ).*

2. ANALYTICAL MODEL FOR NUMERICAL SIMULATION

A typical arrangement between the BS antenna and the RIS can be depicted in Fig. 2, where the coordinates of the BS antenna and RIS generally do not coincide. The radiated EM wave from the BS impinges on the RIS at the incident angles of φ_i and θ_i as a plane wave when the BS-RIS distance is sufficiently far. At each of the RIS unit cells, the incident wave from the BS is reflected at the corresponding specular angles of φ_{mn} and θ_{mn} as shown in the figure, where $m,n \in$ integer indicate the cell location on the RIS. Note that the reflected waves from the RIS’s unit elements are set at different relative phases so that when they are spatially combined, it gives rise to the far-field re-radiation pattern in the desired direction.

2.1 *ANALYSIS MODEL FOR INCIDENT WAVE TO REFLECTED FAR-FIELD PATTERN*

The formulation of the analytical model of the BS-RIS system begins with the calculation of the incident field on the RIS due to the BS antenna. Since the antenna and RIS is generally not coincide as shown in Fig, 2, a coordinate transformation is required. Fig. 3 depicts the relative Cartesian coordinates between the BS antenna and RIS, where they are essentially misaligned by three Eulerian angle rotations α, β and γ as defined in the figure [9]. Typically, the radiated wave from the BS antenna to the RIS is expressed based on its spherical coordinates, s_{BS}. In order to determine the incident wave emanating from the BS arriving at a point on the RIS surface in the Cartesian coordinates, c_{BS}, the spherical to Cartesian transformation is employed as [9],

$$ {}^{c}T^{s} = \begin{pmatrix} \sin\theta_i\cos\varphi_i & \sin\theta_i\sin\varphi_i & \cos\theta_i \\ \cos\theta_i\cos\varphi_i & \cos\theta_i\sin\varphi_i & \sin\theta_i \\ -\sin\varphi_i & \cos\varphi_i & 0 \end{pmatrix}^{-1} . \tag{1} $$

Based on the Eulerian angles between the BS and RIS, the incident field is then transformed from the Cartesian coordinates c_{BS} of the BS to that of the RIS coordinates c'_{RIS} via Eqn. (2).

$$ {}^{c'}A^{c} = \begin{pmatrix} \cos\gamma & \sin\gamma & 0 \\ -\sin\gamma & \cos\gamma & 0 \\ 0 & 0 & 1 \end{pmatrix} \cdot \begin{pmatrix} 1 & 0 & 0 \\ 0 & \cos\beta & \sin\beta \\ 0 & -\sin\beta & \cos\beta \end{pmatrix} \begin{pmatrix} \cos\alpha & \sin\alpha & 0 \\ -\sin\alpha & \cos\alpha & 0 \\ 0 & 0 & 1 \end{pmatrix} \tag{2} $$

Subsequently, the Cartesian coordinates with reference to the RIS coordinates, c'_{RIS}, is employed for computation of the far-field pattern.

Having calculated the incident electric field $\vec{E}_{\mathrm{inc}}(x', y', z')$, the reflected electric field $\vec{E}_{\mathrm{ref}}(x', y', z')$ at the $(m,n)^{th}$ element of the active RIS can be determined as in [10], [11]]:

$$ \vec{E}_{\mathrm{ref}}(x'_m, y'_n, z_0) = A_{RIS}e^{-j\emptyset_{mn}}E_{inc,x}\vec{x}' + G_{ris}e^{-j\emptyset_{mn}}E_{inc,y}\vec{y}' - A_{RIS}e^{-j\emptyset_{mn}}k_{ref,z}^{-1}(k_{ref,x}E_{inc,x} + k_{ref,x}E_{inc,x})\vec{z}' \tag{3a} $$

with

$$ \vec{k}_{\mathrm{ref}}(x'_m, y'_n, z_0) = -k_0(\sin\theta_{mn}\cos\varphi_{mn}\,\vec{x}' + \sin\theta_{mn}\sin\varphi_{mn}\,\vec{y}' - \cos\theta_{mn}\,\vec{z}', \tag{3b} $$

where $\vec{k}_{\mathrm{ref}}$ corresponds to the reflected propagation wave in the specular direction, $k_0 = 2\pi/\lambda_0$ is the phase constant along the propagating direction, θ_{mn} and φ_{mn} are the reflected angles of the plane wave from the $(m,n)^{th}$ element, A_{RIS} is the gain and $\emptyset_{mn}$ is the phase shift associated with the active RIS circuit. Subsequently, the reflected magnetic field $\vec{H}_{\mathrm{ref}}(x', y', z')$ can be calculated as

$$ \vec{H}_{\mathrm{ref}}(x'_m, y'_n, z_0) = \frac{1}{\omega_0\mu_0}\vec{k}_{\mathrm{ref}} \times \vec{E}_{\mathrm{ref}} \tag{4} $$

where ω_0 and μ_0 are the operating radian frequency and permeability in free space, respectively. Note that the above equations are applicable for both X and Y polarization. It is also assumed that there is no cross polarization by the RIS unit cells.

In order to obtain the far-field pattern in the desired direction, the distribution of the phase shift $\emptyset_{mn}$ introduced by the $(m,n)^{th}$ element of the active RIS must be assigned in accordance with the following expression:

$$ \emptyset_{mn} = k_0(d_{mn} - (x_{mn}\cos\theta_{mn} + y_{mn}\sin\varphi_{mn})\sin\theta_{mn}, \tag{5} $$

where d_{mn} is the distance from the BS antenna to the unit element positioned at (x'_m, y'_n, z_0) in the RIS coordinate system. Note that the phase shift and gain of the active RIS circuit will be discussed in the next subsection.

With all the reflected tangential $\vec{E}_{\mathrm{ref}}$ and $\vec{H}_{\mathrm{ref}}$ fields being calculated, and the phase shift associated with all the unit elements being assigned, the reflected far-field pattern reradiated from the planar RIS aperture at the distance r can be computed with the use of the First Principle Equivalence as given below [10]:

$$ E_\theta = +\frac{jk_0\,exp(-jk_0r)}{4\pi r}\left(P_x\,cos\,\varphi + P_y\,sin\,\varphi - \eta_0\,cos\,\theta\left(Q_x\,sin\,\varphi - Q_y\,cos\,\varphi\right)\right) \tag{6a} $$

$$ E_\varphi = -\frac{jk_0\,exp(-jk_0r)}{4\pi r}\left(\eta_0\left(Q_x\,cos\,\varphi + Q_y\,sin\,\varphi\right) + cos\,\theta\left(P_x\,sin\,\varphi - P_y\,sin\,\varphi\right)\right) \tag{6b} $$

with

$$ P_{x,y}(u,v) = a\,b\,\mathrm{sinc}\left(\frac{k_0ua}{2}\right)\mathrm{sinc}\left(\frac{k_0vb}{2}\right)\cdot \sum_m\sum_n E_{\mathrm{ref},x,y}(x_m, y_n)\,e^{jk_0(ux_m+vy_n)} \tag{7a} $$

$$ Q_{x,y}(u,v) = a\,b\,\mathrm{sinc}\left(\frac{k_0ua}{2}\right)\mathrm{sinc}\left(\frac{k_0vb}{2}\right)\cdot \sum_m\sum_n H_{\mathrm{ref},x,y}(x_m, y_n)\,e^{jk_0(ux_m+vy_n)} \tag{7b} $$

where $u = \sin\theta_{mn}\cos\varphi_{mn}$ and $v = \sin\theta_{mn}\sin\varphi_{mn}$, a and b are the unit cell's dimension. Note that $P_{x,y}$ and $Q_{x,y}$ are the spectrum functions, which can be efficiently calculated via the inverse fast Fourier transform (IFFT) algorithm. For the H field, it can be determined from the E field via the free space impedance $\eta_0 = \sqrt{\mu_0/\epsilon_0}$.

2.2 MODELING OF ACTIVE RIS UNIT CELL

Fig. 3 (a)-(b) depict two typical circuit schematics for the unit cell of an active RIS. It typically consists of an antenna (ANT), a passive phase shifter (PS), and a reflection amplifier (RA). The PS and RA can be configured in parallel or in cascade connection as illustrated in the figure. The RA is typically represented by a negative conductance, $-G_{RIS}$ $(G_{RIS} > 0)$.

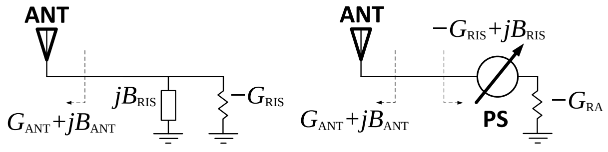

(a) (b)

Fig. 3 *Active RIS circuit model (a) parallel and (b) cascade configuration.*

In operation, the antenna converts the impinging EM waves to an electrical signal propagating toward the PS and RA. Due to the difference between the impedances or admittances of the ANT and the PS-RA circuit, the signal undergoes a reflection and hence propagates backward to the antenna before re-radiating as a reflected EM wave out of the unit cell. Note that the magnitude and phase of the reflected EM wave can be controlled by the phase shift and the amplifying gain associated with the PS-RA circuit. This can be modelled by a one-port admittance $Y_{RIS} = Y_{PSRA} = -G_{RA} + jB_{PS}$, with a negative real part $-G_{RA}$. By putting the antenna admittance as $Y_{ANT} = G_{ANT} + jB_{ANT}$, the reflection coefficient Γ_{RIS} of the unit cell can be expressed as

$$\Gamma_{RIS} = \frac{Y_{ANT}-Y_{PSRA}}{Y_{ANT}+Y_{PSRA}} = \frac{(G_{ANT}+G_{RA})+j(B_{ANT}-jB_{PS})}{(G_{ANT}-G_{RA})+j(B_{ANT}+jB_{PS})} \tag{8}$$

The gain of the active RIS is attributed to the denominator term $(G_{ANT} - G_{RA})$ in the equation. It is important that the term $(G_{ANT} - G_{RA})$ must always be kept positive over the operating range and frequencies so as to ensure stability.

For low noise and low power operation, the PS and RA are typically of an LC passive and a positive feedback amplifier types, respectively [11] - [14]. Following this and Eqn.(8), the sources of gain and phase variations in the reflection coefficient of the active RIS include 1) the antenna admittance Y_{ANT}, 2) the input admittance $-G_{RA}$ of the RA, and the admittances jB_{PS} associated with the PS. Note that the extent of such errors is dependent on the choices of circuit implementation.

3. SIMULATION RESULTS AND DISCUSSION

Based on the analysis equations and procedures outlined in Section 2, the performances of the active RIS can now be evaluated. The physical and electrical setups for the RIS can be summarized as follows. The operating center frequency is at 28GHz in accordance with the frequency band of 5G NR. The distance from the BS to the RIS is 10 meters, where the incident *plane* wave arrives at the RIS is at the θ_i = 20^{o} and φ_i = 70^{o} with reference to the spherical coordinates of the RIS. The reflected far field pattern of from the RIS was computed at 10 meters with the desired direction at θ_r = 30^{o} and φ_r = 10^{o}. For simulation, the size of the RIS was varied from N_{ris} = 8×8 = 64 unit cells to N_{ris} = 16×16 = 256 unit cells, whereas the number of phase resolutions were set at B_{ph} = 1, 2 and 3 bits. The size of each unit element was set at half of the wavelength at 28GHz. The impact of the gain and phase errors attributed from the unit cells was assessed by virtue of Monte-Carlo simulation. Without loss of generality, the gain of the active RIS, A_{aRIS}, is normalized with a uniform random error distribution at ±1.5dB, whereas the phase error is set at ±25% from their corresponding nominal values. It is assumed that such variation is within the range of practical errors in real circuit implementation. A total of 250 runs was performed for each setup of the RIS parameter.

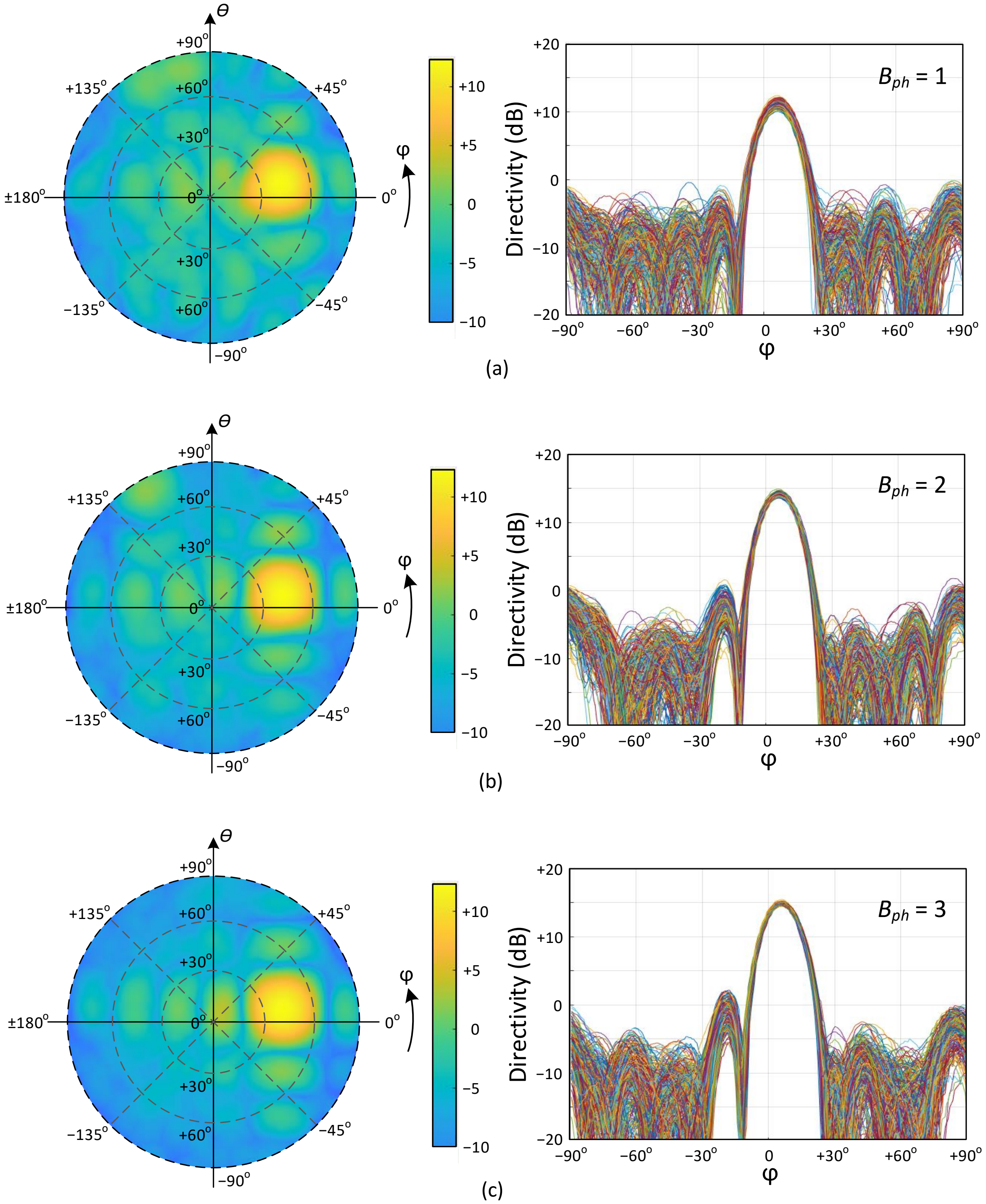

Fig. 4 *2-D and 1-D directivity plots of active RIS at N_{ris} = 64 unit cells with B_{ph} = (a) 1 bit (b) 2 and (c) 3 bits.*

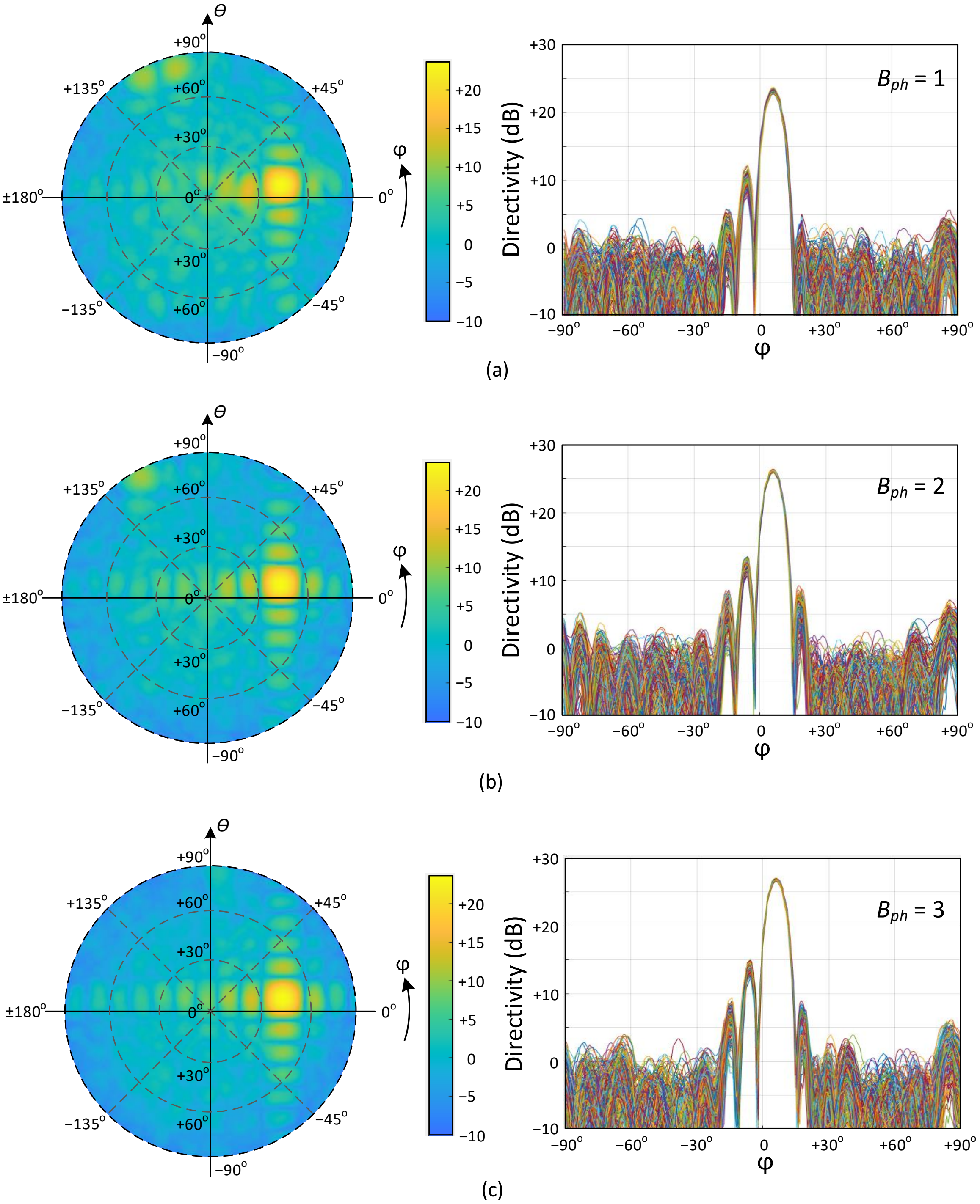

(a)

(b)

(c)

***Fig. 5** 2-D and 1-D directivity plots of active RIS at N_{ris} = 256 unit cells with (a) B_{ph} = 1 bit (b) 2 and (c) 3 bits.*

Fig. 4 and 5 show the reflected far-field radiation patterns of the RIS, in form of both contour and line plots along the θ-φ coordinates, at different number of phase resolutions B_{ph} = 1, 2 and 3, and number of unit cells N_{ris} = 64 and 256. It is evident in all cases that the incident wave was reflected to the direction close to θ = 30° and φ = 10°, with some discrepancies due to the phase quantization from the calculated phase distribution in (6).

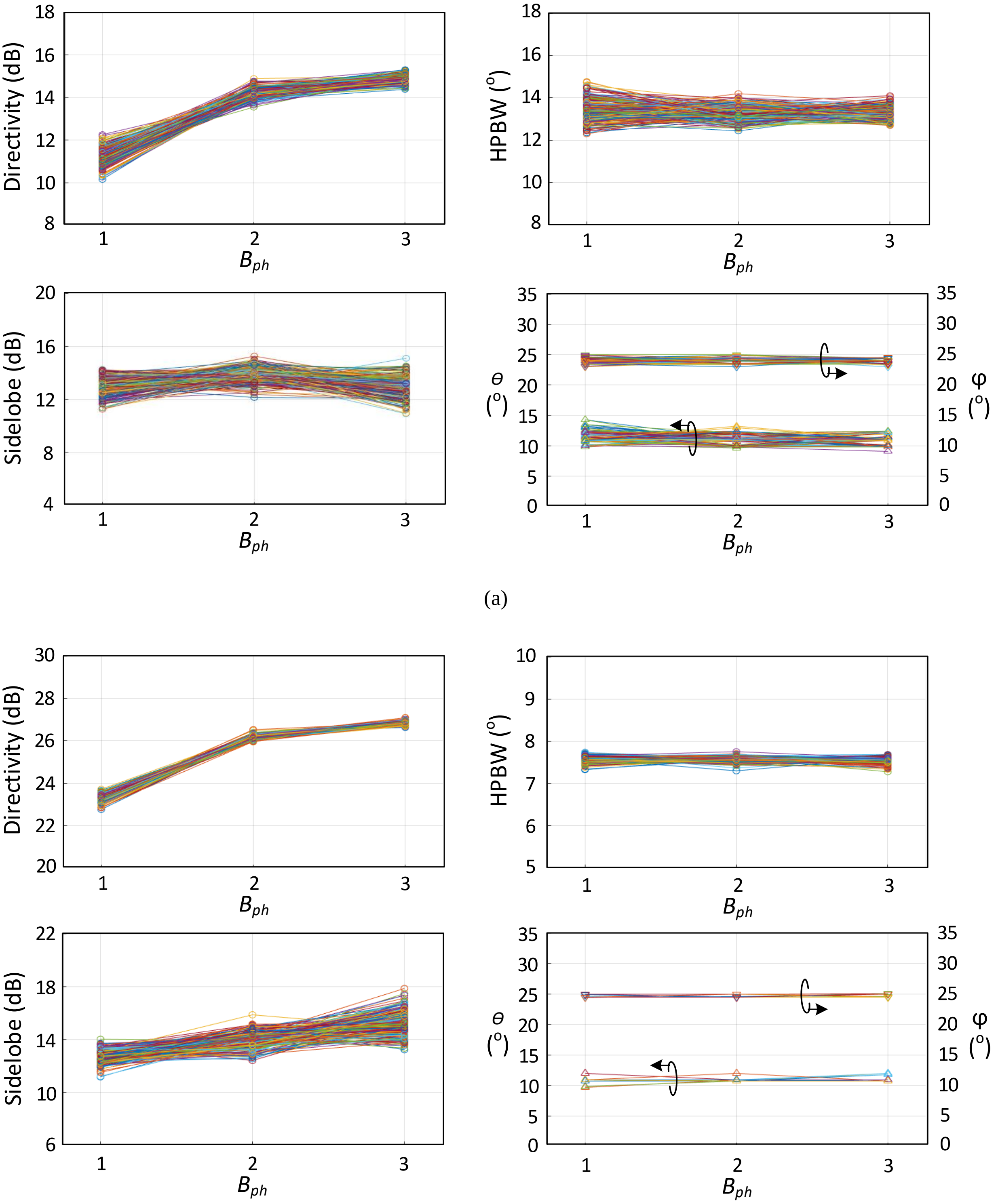

(a)

(b)

Fig. 6 RIS performance variation against number of bits B_{ph} at (a) N_{ris} = 64 and (b) N_{ris} = 256.

Consider the contour plots in the figures at N_{ris} = 64 and 256. As the phase resolution B_{ph} increases, the overall side-lobe is more suppressed since more proportion of the contour area becomes blue color, indicating a low field level (see the color bar on the side of each plot). Now consider the directivity plots on the right side. As B_{ph} increases, the peak directivity in the steered far-field direction increases whereas the half-power beamwidth (HPBW) remains practically intact. It is also noticed that the variations in the peak directivity and HPBW due to the gain/phase errors become less. In addition, an increase in the RIS size (from N_{ris} = 64 to 256 in Fig. 4 and 5, respectively) results in a higher peak directivity and a smaller HPBW, as expected.

Considering the impact of the gain/phase errors from the figures, it is clearly seen that a larger RIS size and a higher phase resolution in the RIS can suppress variations in the peak directivity and HPBW performances.

In order to investigate more quantitatively the robustness against the gain/phase errors of the RIS with a larger size N_{ris} and higher phase resolution B_{ph}, Monte-Carlo plots of the RIS performances, including the peak directivity, HPBW, steered angles, and minimum side-lobe suppression, are given in Fig. 6 and 7 for N_{ris} = 64 and 256, respectively. From the figures, with B_{ph} varied from 1 to 3 bits, the peak directivity increases by 3.6 dB and 3.4 dB, and minimum side-lobe suppression by 0 dB and 2.4 dB for N_{ris} = 64 and 256, respectively. On the other hands, the steered angles and HPBW are maintained. Consider variations in the performance due to the directivity/phase errors. At N_{ris} = 64, the peak directivities are varied by 2.1 dB at B_{ph}= 1, side-lobe suppression by 2.9 dB at B_{ph}= 3, HPBW by 2.1^{o} at B_{ph}= 1, and steered angles by 4.9^{o} at B_{ph}= 1. At N_{ris} = 256, it is evident that the variations are suppressed where the peak directivities are varied by 2.0 dB at B_{ph}= 1, side-lobe suppression by 4.2 dB at B_{ph}= 3, HPBW by 0.8^{o} at B_{ph}= 1, and steered angles 2.2^{o} at B_{ph}= 1. These thereby confirm the performance trend as already observed from Fig. 4 and 5.

4. CONCLUSION

A numerical performance investigation of the active reconfigurable intelligent surface (RIS) has been presented based on analytical equations. With practical gain and phase variations associated with the antenna impedance, reflection amplifier and phase shifter circuits included, it is clearly shown via Monte-Carlo simulation that the RIS performance becomes more robust as the size and phase resolution increase. Also evident is the fact that the benefit of an improved robustness becomes diminished with the increasing size and resolution. From the simulated results in Fig. 6 with a specific gain error at 3dB and a phase variation at $\pm 25^{o}$, the RIS with 256 elements and 2-bits should be sufficient to provide over 25-dB normalized peak directivity, less than 8^{o} HPBW, more than 12-dB minimum side-lobe suppression and very low steered angle error. Given realistic circuit errors in a specific RIS implementation, such numerical computation should be useful as a design guideline in practice.

REFERENCES

[1] M. Di Renzo, A. Zappone, M. Debbah, M. S. Alouini, C. Yuen, J. de Rosny, and S. Tretyakov, “Smart radio environments empowered by reconfigurable intelligent surfaces: How it works, state of research, and the road ahead,” IEEE J. Sel. Areas Commun., vol. 38, no. 11, pp. 2450– 2525, Nov. 2020

[2] L. Zhang, X. Q. Chen, S. Liu, Q. Zhang, J. Zhao, J. Y. Dai, G. D. Bai, X. Wan, Q. Cheng, G. Castaldi, V. Galdi, and T. J. Cui, “Spacetime-coding digital metasurfaces,” Nat. Commun., vol. 9, no. 4338, Oct. 2018

[3] C. Huang, R. Mo, and C. Yuen, “Reconfigurable intelli-gent surface assisted multiuser MISO systems exploiting deep reinforcement learning,” IEEE J. Sel. Areas Commun., vol. 38, no. 8, pp. 1839–1850, Aug. 2020

[4] J. -B. Gros, V. Popov, M. A. Odit, V. Lenets and G. Lerosey, "A Reconfigurable Intelligent Surface at mmWave Based on a Binary Phase Tunable Metasurface," in IEEE Open Journal of the Communications Society, vol. 2, pp. 1055-1064, 2021.

[5] W. Tang et al., "Path Loss Modeling and Measurements for Reconfigurable Intelligent Surfaces in the Millimeter-Wave Frequency Band," in IEEE Transactions on Com-munications, vol. 70, no. 9, pp. 6259-6276, Sept. 2022.

[6] Q. Wu and R. Zhang, "Intelligent Reflecting Surface Enhanced Wireless Network via Joint Active and Passive Beamforming," in IEEE Transactions on Wireless Communications, vol. 18, no. 11, pp. 5394-5409, Nov. 2019.

[7] R. Long, Y. -C. Liang, Y. Pei and E. G. Larsson, "Active Reconfigurable Intelligent Surface-Aided Wireless Communications," in IEEE Transactions on Wireless Communications, vol. 20, no. 8, pp. 4962-4975, Aug. 2021.

[8] Z. Zhang et al., "Active RIS vs. Passive RIS: Which Will Prevail in 6G?," in IEEE Transactions on Com-munications, vol. 71, no. 3, pp. 1707-1725, March 2023.

[9] Y. Rahmat-Samii, "Useful coordinate transformations for antenna applications," in IEEE Transactions on Antennas and Propagation, vol. 27, no. 4, pp. 571-574, July 1979.

[10] D. R. Prado et al., "Efficient Crosspolar Optimization of Shaped-Beam Dual-Polarized Reflectarrays Using Full- Wave Analysis for the Antenna Element Characterization," in IEEE Transactions on Antennas and Propagation, vol. 65, no. 2, pp. 623-635, Feb. 2017.

[11] Imaz-Lueje, B., Prado, D.R., Arrebola, M. *et al.* Reflect-array antennas: a smart solution for new generation satellite mega-constellations in space communications. *Sci Rep* **10**, 21554 (2020).

[12] J. -F. Bousquet, S. C. Magierowski and G. G. Messier, "An Integrated Active Reflector for Phase-Sweep Cooperative Diversity," in IEEE Transactions on Circuits and Systems II: Express Briefs, vol. 56, no. 8, pp. 624-628, Aug. 2009.

[13] S. J. Thomas, E. Wheeler, J. Teizer and M. S. Reynolds, "Quadrature Amplitude Modulated Backscatter in Passive and

Semipassive UHF RFID Systems," in IEEE Transactions on Microwave Theory and Techniques, vol. 60, no. 4, pp. 1175-1182, April 2012.

[14] J. Kimionis, A. Georgiadis, A. Collado and M. M. Tentzeris, "Enhancement of RF Tag Backscatter Efficiency With Low-Power Reflection Amplifiers," in IEEE Transactions on Microwave Theory and Techniques, vol. 62, no. 12, pp. 3562-3571, Dec. 2014.

Apisak Worapishet received the B.Eng. (Hons.) degree from the King Mongkut’s 1270 Institute of Technology Ladkrabang, Bangkok, Thailand, in 1990, the M.Eng.Sc. degree from the University of New South Wales, Kensington, NSW, Australia, in 1995, and the Ph.D. degree from the Imperial College London, London, U.K., in 2000, all in electrical engineering.

Since 1990, he has been with the Mahanakorn University of Technology, Bangkok, Thailand, where he is currently a Professor of electronic engineering. He is also the director of the Mahanakorn Microelectronics Research Center and a Lecturer with the Mahanakorn Institute of Innovation, Bangkok, Thailand. His research interests include analogue integrated circuits, passive/active RF/microwave circuits, and wireless power transfer.

From 2016 to 2023, Dr. Worapishet served an Associate Editor for the IEEE TRANSACTIONS ON CIRCUITS AND SYSTEMS I: REGULAR PAPERS. He was the Editor-in-Chief for ECTI Transactions on Electrical Engineering, Electronics, and Communications from 2012 to 2019. He was the recipient of the British Council Researcher Exchange Program Award in 2009. He is now a Visiting Professor at the RFIC design laboratory at University College Dublin. He is an IEEE Senior member and a member of the Analog Signal Processing Technical Committee and the IEEE Circuits and Systems Society.